Thermal Gradient Mechanical Fatigue, Hardness, Adhesive Strength, and Erosion Resistance of Layered $La_2Zr_2O_7$ Thermal Barrier Coatings

Xingye Guo[a,d], Li Li[b], Hyeon-Myeong Park[c], James Knapp[b], Yeon-Gil Jung[c*], Jing Zhang[a]*

a Department of Mechanical Engineering, Indiana University-Purdue University Indianapolis, IN 46202, USA

b Praxair Surface Technologies Inc., Indianapolis, IN 46222, USA

c School of Materials Science and Engineering, Changwon National University, Changwon, Kyungnam 641-773, Republic of Korea

d College of Materials Science and Engineering, Beijing University of Technology, Beijing, 100124, China

*Corresponding Authors: jz29@iupui.edu; jungyg@changwon.ac.kr

Abstract

Lanthanum zirconate ($La_2Zr_2O_7$) has been proposed as a promising thermal barrier coating (TBC) material due to its low thermal conductivity and high stability at high temperatures. In this work, both single and double ceramic layer (DCL) TBC systems of $La_2Zr_2O_7$ and 8 wt % yttria-stabilized zirconia (8YSZ) have been prepared using air plasma spray (APS) technique. The thermomechanical properties and microstructures were investigated. Thermal gradient mechanical fatigue (TGMF) tests were applied to investigate the thermal cycling performance. The results show that the DCL $La_2Zr_2O_7$ + 8YSZ TBC

This is the author's manuscript of the article published in final edited form as:
Guo, X., Li, L., Park, H.-M., Knapp, J., Jung, Y.-G., & Zhang, J. (2018). Mechanical Properties of Layered La2Zr2O7 Thermal Barrier Coatings. Journal of Thermal Spray Technology, 27(4), 581–590. https://doi.org/10.1007/s11666-018-0703-5

samples have fewer number of cycles than that of single-layer 8YSZ TBC samples in the TGMF tests. This is because DCL $La_2Zr_2O_7$ TBC samples have higher residual stress during thermal cycling process, and their fracture toughness are lower than that of 8YSZ. Adhesive strength test results show that 8YSZ TBC samples have a higher adhesive strength than that of $La_2Zr_2O_7$. The erosion rates of $La_2Zr_2O_7$ TBC samples are higher than that of 8YSZ, due to the lower critical erodent velocity and fracture toughness of $La_2Zr_2O_7$. The DCL porous 8YSZ + $La_2Zr_2O_7$ had a lower erosion rate than other SCL and DCL $La_2Zr_2O_7$ coatings, suggesting porous 8YSZ serves as a stress relief buffer layer.

Keywords: Thermal barrier coating; Lanthanum zirconate; Thermal cycling; Adhesive strength; Erosion.

1. Introduction

Thermal barrier coating (TBC) materials with low thermal conductivities have been widely used to insulate turbine and engine components from hot gas stream in high-temperature environments [1]. TBC systems typically consist of a superalloy substrate, a metallic bond coat layer, a thermal grown oxide (TGO) layer, and a low thermal conductivity ceramic top coat. The criteria for TBCs material selection include low thermal conductivity, high melting point, high thermal expansion coefficient, good thermal and chemical stability, no phase change, and low sintering activity [1]. Since the maximum surface temperature of commercial 8 wt% yttrium stabilized zirconia (8YSZ) TBCs is limited to 1200 ^{o}C due to potential sintering and phase change [2, 3], recently lanthanum zirconate ($La_2Zr_2O_7$) has been proposed as an alternative TBC material in higher temperature applications. Compared with 8YSZ, $La_2Zr_2O_7$ (1.5 W/m-K) has a lower thermal conductivity than that of 8YSZ (2.2 W/m-K) [3, 4], and it has no phase change from room temperature to its melting temperature (2300 ^{o}C) [5-7]. The thermal expansion coefficient of $La_2Zr_2O_7$ is 9.1×10^{-6} K^{-1}, which is slightly lower than 8YSZ (11×10^{-6} K^{-1}) [6-8].

Vassen *et al.* studied the thermal, mechanical properties and thermal stability of hot pressed fully dense $La_2Zr_2O_7$ [7]. The Young's modulus of hot pressed $La_2Zr_2O_7$ was lower than YSZ. The fracture toughness was comparable to air plasma sprayed YSZ. Thermal conductivity of $La_2Zr_2O_7$ was about 20% lower than YSZ [7]. Vassen *et al.* also compared the thermal cycling performances between the air plasma sprayed double-ceramic layer (DCL) and single-ceramic layer (SCL) $La_2Zr_2O_7$ TBC samples [6]. The DCL TBCs samples, which included $La_2Zr_2O_7$ and YSZ, had similar cycling performance as SCL YSZ coating at temperatures below 1300 ^{o}C. At higher temperatures, the DCL TBC samples

revealed an excellent thermal cycling behavior [6]. Wang *et al.* studied a $La_2Zr_2O_7$/8YSZ functionally graded coating, which showed an improved performance in thermal cycling tests compared to SCL $La_2Zr_2O_7$ and DCL $La_2Zr_2O_7$/8YSZ [9]. In another study, Liu *et al.* showed that the thermal and mechanical properties (microhardness and elastic modulus) and thermal conductivity of plasma sprayed $La_2Zr_2O_7$ coating were remarkably increased after 20 hours heat treatment due to sintering effect [10]. The adhesive strength of plasma sprayed $La_2Zr_2O_7$ coating decreased with increasing porosity. Sivakumar *et al.* reported that the adhesive strengths were 6.63 MPa, 6.17 MPa, and 3.73 MPa, which corresponded to the plasma sprayed $La_2Zr_2O_7$ coatings with the porosity of 16%, 21% and 28%, respectively [11]. Lyu *et al.* investigated the cycling performance of $La_2Zr_2O_7$/8YSZ composite coating in TGMF tests, and indicated that $La_2Zr_2O_7$/8YSZ buffer layer improved the TGMF cycling performance [12]. A few recent reviews of $La_2Zr_2O_7$ based coating materials were given by Bakan [13] and Zhang [14].

To analyze the failure mode and the mechanisms, Wang *et al.* calculated the residual stress using a finite element model with the birth and death element technique [15]. The results showed that there was a stress concentration on the surface and at the edge of the coating. The double layered $La_2Zr_2O_7$/8YSZ coating had a lower residual stress than the single layered 8YSZ coating.

In terms of erosion resistance, Cernuschi *et al.* studied the erosion resistance of plasma sprayed YSZ, $Gd_2Zr_2O_7$ and Yttrium Aluminum Garnet (YAG) coatings [16]. The results showed that the YAG coating demonstrated the best erosion resistance. Additionally, the erosion rates were related to both coating materials and the kinetic energy of erodent particles.

Previous studies were mainly focused on the thermal and physical properties of $La_2Zr_2O_7$, and only limited works have been done on the mechanical properties, which are equivalently important to thermal properties, and coupled thermomechanical properties of the air plasma sprayed $La_2Zr_2O_7$ coatings. This paper will focus on three specific mechanical relevant properties: thermal gradient mechanical fatigue, adhesive strength, and erosion resistance properties of $La_2Zr_2O_7$ based coatings. The TGMF test is a novel method to evaluate the coating thermal cycling behaviors under mechanical load, which is especially critical to turbine blades which are subjected to stress from centrifugal force. Turbine stages can rotate at tens of thousands of revolutions per minute, and fluid forces can cause fracture, yielding, or creep failures. An accurate understanding of how turbine blades behave in service conditions under a variety of temperature and stress load is warranted.

The objective of this study is to provide the thermomechanical property data for the $La_2Zr_2O_7$ TBC specimens. In this work, both single layered and double layered $La_2Zr_2O_7$ TBC specimens were prepared using air plasma spray technique. 8YSZ TBC specimen was also fabricated for comparison proposes. Thermal gradient mechanical fatigue tests were conducted to evaluate the thermomechanical properties. Vickers hardness and porosity were measured. Adhesive strength tensile tests were employed to investigate the interfacial properties of the coatings. An analytical model was used to estimate the stress distribution in the coatings, which explains the observed fracture behavior in the adhesive strength tensile test. Finally erosion tests were performed to evaluate the coatings erosion resistance. A new model of using critical velocity as an alternative of conducting erosion test is proposed.

2. Experimental procedure

Both $La_2Zr_2O_7$ and 8YSZ coatings were sprayed by APS method using a Praxair's proprietary plasma torch (Praxair Surface Technologies Inc., Indianapolis, Indiana). Haynes 188 (Haynes International, Inc., Kokomo, Indiana) superalloy was used as the substrate. Prior to the spraying, the substrates were sandblasted using alumina grits and cleaned by ethanol. A Ni-based metallic material, LN-65, patented by Praxair, was used as the bond coat, and was also deposited using APS method. The spray conditions are current 150 ~250 A, voltage ~100 V, standoff distance ~50 mm, powder feed rate 30~60 g/min. The architectures and thicknesses of the sprayed top coatings are listed in Table 1.

Table 1. $La_2Zr_2O_7$ and YSZ top coatings

Sample #	Top coat	Top coat thickness (μm)
1	SCL porous $La_2Zr_2O_7$	430 ± 56
2	SCL porous 8YSZ	432 ± 32
3	DCL porous 8YSZ & $La_2Zr_2O_7$	130 ± 37 & 303 ± 49
4	DCL dense 8YSZ & $La_2Zr_2O_7$	127 ± 43 & 305 ± 51

In order to measure the hardness, TGMF, adhesive strength, and erosion resistance, four different shapes of substrate were used. These substrates were made of Haynes 188 superalloy. The 10×10×10 mm cubes were used to produce free standing samples. The top coats were deposited directly on smooth cube substrates without a bond coat. The round button substrates with a diameter of 1 inch (25.4 mm in diameter) were used in the adhesive

strength. Tensile bar samples (200×20×3 mm) were used in the TGMF tests. Rectangular panel (50.8×25.4×3 mm) samples were used in the erosion tests.

The porosities of free standing samples were measured following the ASTM standard B328-94. The measurement apparatus includes an analytical balance (Mettler AE240, Switzerland) and a density determination kit (Denver Instrument, Arvada, Colorado). Vickers hardness tests were conducted on the cross section of the TBC specimens using a Vickers hardness tester (Mitutoyo Corp., HM−114, Japan). The load of the hardness measurement was 1 kgf (9.807 N), the load rate was 60μm/s, and the dwell time was 10 s. Five indentations were conducted for each sample to get statistics.

The TBC cross sectional microstructures were observed using scanning electron microscope (SEM, JEOL, JSM−5610, Japan) after sample preparation. The samples were cold mounted in a vacuum chamber using epoxy resin. Using cold mount in vacuum, epoxy can impregnate into the pores and cracks of the TBCs, which provides a good support to the porous material without damaging the microstructures.

The thermal gradient mechanical fatigue test combines thermal exposure and mechanical loading test, which introduces a thermal gradient across a tensile bar [17]. As shown in Fig. 1, the samples were heated to 850 ^{o}C or 1100 ^{o}C for 10 minutes on the top coating front side, and kept at a constant temperature of 350 ^{o}C on the back side. The samples were cooled on the front surface using a compressed air for 3 minutes and then ambient cooling for 7 minutes. A constant tensile load of 150 N was applied to the tensile bar. The heating and cooling profile and tensile load are shown in Fig. 2.

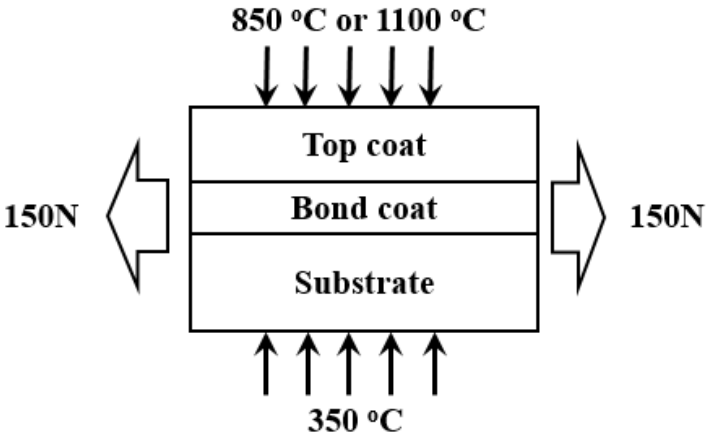

Fig. 1. Schematic of TGMF test showing tensile load and thermal conditions.

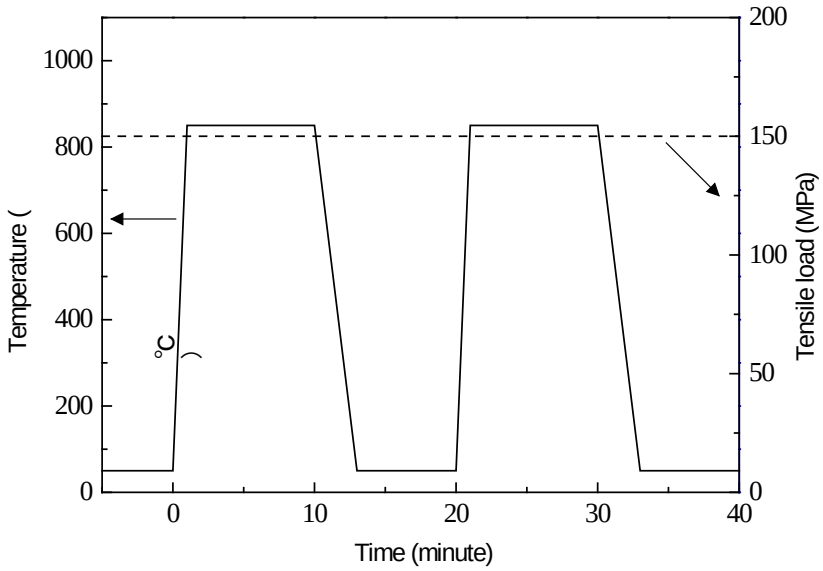

Fig. 2. The heating and cooling profile in the TGMF test.

Sufficient adhesive strength between coating layers is critical to TBC systems, since durability and integrity of coating depend on the adhesive strength. Adhesive strength

experiments were conducted. The loading speed of the adhesive strength test was controlled at 1.27 mm/min (0.05 inch/min). Epoxy (FM 1000 adhesive film) was used to glue the TBC top coatings to two steel cylinders. The bonding agent is capable of bonding the coating to the loading fixture with a tensile strength which is greater than the minimum required adhesion strength of the coating. Additionally, FM 1000 has sufficient viscosity to prevent penetrating into the coating.

Erosion resistance tests were performed following the ASTM G76-13 standard. Aluminum oxide sand with an average particle size of 50 μm was used as the erosive material. Total 600 g of sands were used for each sample. Compressed air was used as the carrier gas. The rate of sand flow stream was 6 g/s at an impingement angle of 20^{o}. The impingement velocity of the particle could reach to a range of 300-400 m/s. The erosion rate (mg/g) was used to evaluate the erosion resistance, which was calculated by dividing the TBC erosion weight by the abrasive flow weight.

3. Results and discussion

3.1 Porosity and hardness measurements

The measured average density and porosity of $La_2Zr_2O_7$ were 5.31 g/cm^3 and 12.27 %, respectively; and the porosity of porous 8YSZ samples was in the same level as porous $La_2Zr_2O_7$. The Vickers hardness of porous 8YSZ coatings was similar as $La_2Zr_2O_7$ coatings, as shown in Fig. 3 . However the hardness of dense 8YSZ coating was much higher than other coatings, due to its low porosity.

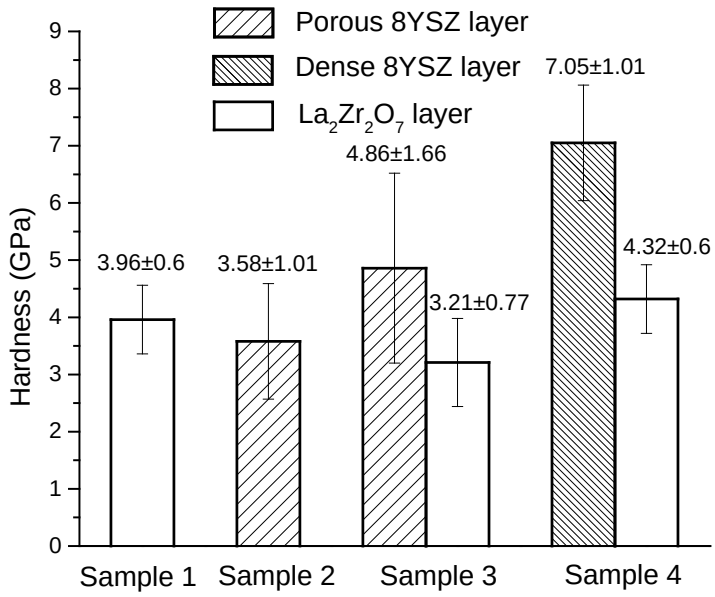

Fig. 3. Vickers hardness in different layers of TBC samples.

3.2 Thermal gradient mechanical fatigue test

TGMF tests were conducted in two different temperature gradient environments. The first set of specimens was heated to 850 ^{o}C on the front side and kept 350 ^{o}C on the back side. The second set of specimens was heated to 1100 ^{o}C on the front side and kept 350 ^{o}C on the back side.

Fig. 4 shows the optical images of the samples before and after the TGMF tests heated at 850 ^{o}C. As shown in Fig. 4 (a) and (b), after 1200 cycles, there was no crack or spallation tendency in the single layered porous 8YSZ coatings. As shown in Fig. 4 (b) ~ (f), the double layered $La_2Zr_2O_7$ can't last many cycles. In Fig. 4 (c) and (d), the double layered porous 8YSZ and $La_2Zr_2O_7$ coatings (sample 3) delaminated on the edge after 220 cycles. In

Fig.4 (e) and (f), the double layered dense 8YSZ and $La_2Zr_2O_7$ coatings delaminated after 50 cycles.

(a)

(b)

(c)

(d)

(e)

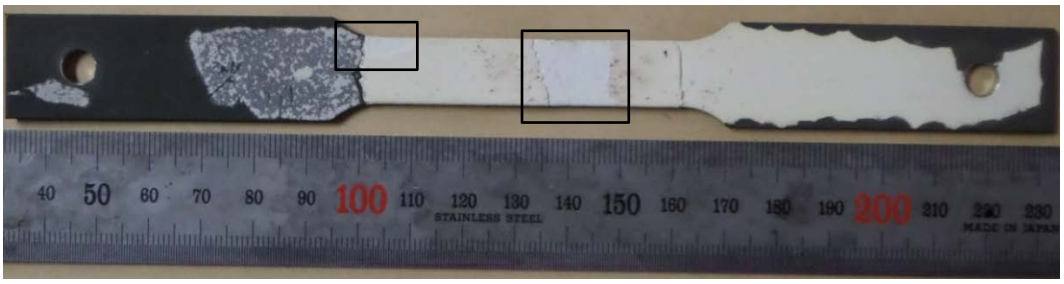

(f)

Fig. 4. Optical images of the TBC samples before and after the first set TGMF tests heated at 850 ^{o}C: (a) sample #2, as-sprayed SCL porous 8YSZ TBCs, (b) sample #2, SCL porous 8YSZ TBCs after 1200 TGMF cycles, (c) sample #3, as-sprayed DCL porous 8YSZ+ $La_2Zr_2O_7$, (d) sample 3, DCL porous 8YSZ+ $La_2Zr_2O_7$ after 220 TGMF cycles, (e) sample #4, as-sprayed DCL dense 8YSZ+ $La_2Zr_2O_7$, and (f) sample #4, DCL dense 8YSZ + $La_2Zr_2O_7$ after 50 TGMF cycles. Blocks highlight the failure sites.

The optical images of TBC samples before and after the second set TGMF tests heated at 1100 ^{o}C are shown in Fig. 5. As shown in Fig. 5 (b), both 8YSZ and $La_2Zr_2O_7$ layer were partially delaminated near the center of the tensile bar after 38 cycles. Part of bond coat was exposed due to the delamination. Figure 5 (d) shows that only the top $La_2Zr_2O_7$ layer was delaminated after 49 cycles. Comparing with the first set TGMF tests, both sample 3 and sample 4 had shorter lifecycles in second set. The DCL porous 8YSZ + $La_2Zr_2O_7$ had better performance in lower temperature gradient in first set TGFM tests, and became worse with higher temperature gradient in second set tests.

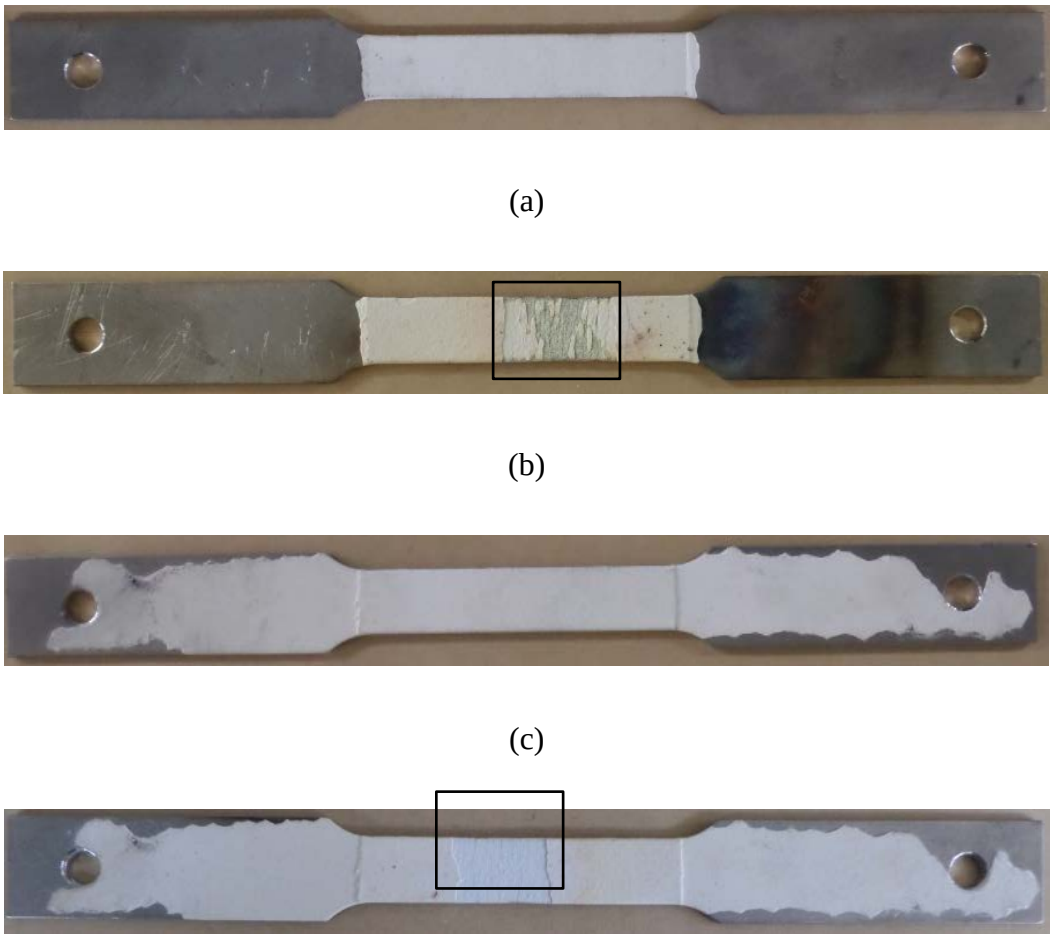

(a)

(b)

(c)

(d)

Fig. 5. Optical images of the TBC samples before and after the second set TGMF tests heated at 1100 ^{o}C: (a) sample #3, as-sprayed DCL porous 8YSZ+ $La_2Zr_2O_7$, (b) sample #3, DCL porous 8YSZ+ $La_2Zr_2O_7$ after 38 TGMF cycles, (c) sample #4, as-sprayed DCL dense 8YSZ+ $La_2Zr_2O_7$, and (d) sample #4, DCL dense 8YSZ + $La_2Zr_2O_7$ after 49 TGMF cycles. Blocks highlight the failure sites.

Typically the spallation process starts at the edges between $La_2Zr_2O_7$ coating and 8YSZ coating sublayer. In this TGMF experiment, all the spallation occurred near the interface

between the $La_2Zr_2O_7$ layer and 8YSZ layers, which was just underneath the $La_2Zr_2O_7$ top coating. The first stage of the spallation process was the buckling of the $La_2Zr_2O_7$ top coating layer, followed by the occurrence of cracks at the interface. The second stage was the propagation of cracks at the interface, which was followed by the spallation of top coat. Finally, the flakes of the $La_2Zr_2O_7$ top coating peeled off [18].

Because the coefficients of thermal expansion (CTE) of 8YSZ (11×10^{-6} K^{-1} at 1000 ^oC) are about 20% large than $La_2Zr_2O_7$ (9×10^{-6} K^{-1} at 1000 ^oC) [6, 19], the volume expansion difference is very large between the 8YSZ and $La_2Zr_2O_7$ layers, and thermal stress is induced during thermal cycling. According to Evans's theory, when the thermal stress sufficiently succeeds the yield strength of the coating material, the undulation imperfections at the coating interface flow plastically from the base to the peak, allowing the amplitude of the undulation to increase [20]. Therefore, in this work, thermal stresses around these imperfections initiated the interfacial separation of the coatings. Additionally, since the fracture toughness of $La_2Zr_2O_7$ is lower than that of 8YSZ [7, 21], DCL 8YSZ and $La_2Zr_2O_7$ coatings tended to spall first in the $La_2Zr_2O_7$ layers near the interface.

3.3 Adhesive strength test

Single layered coating samples were investigated for adhesive strength test. Because the adhesive strength is affected by various interfaces and layers in multi-layer coatings, it is difficult to determine the adhesive strength at specific interface for DCL TBCs.

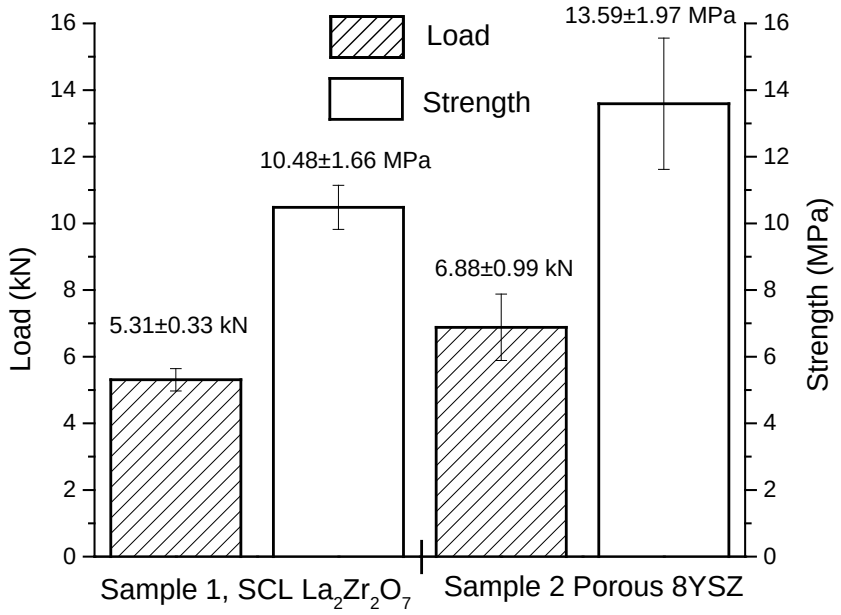

Fig. 6. Load and adhesive strength values for single layered coating samples.

As shown in Fig. 6, the tensile load and adhesive strength of 8YSZ samples were higher than those of $La_2Zr_2O_7$. The adhesive strength was calculated by dividing the tensile load with the cross section area of the tensile bar samples. The difference in the tensile load and adhesive strength is primarily caused by fracture toughness [22]. Previous studies have showed that $La_2Zr_2O_7$ standing coatings have a lower fracture toughness than that of 8YSZ coatings (2.2~3.3 $MPa \cdot m^{½}$ for 8YSZ, and 1.1 $MPa \cdot m^{½}$ for $La_2Zr_2O_7$), suggesting $La_2Zr_2O_7$ coatings are prone to fracture under tensile load [7, 21, 23]. Therefore, $La_2Zr_2O_7$ TBC samples are expected to have lower adhesive strength than that of 8YSZ.

Fig. 7 shows the cross sectional SEM images of the TBC systems before and after the adhesive strength tests. As shown in Figs. 7a and 7b, even though the porosities of $La_2Zr_2O_7$ and 8YSZ coatings were similar before the adhesive est, the $La_2Zr_2O_7$ coating samples had scattered ‘splats’ grain and net-shape cracks. Therefore, during the adhesive tests, the cracks were easily to propagate along the boundaries, as shown in Figs. 7c and 7d. However, the 8YSZ coatings showed fewer boundaries but much larger pores than $La_2Zr_2O_7$. There were fewer crack initiation sites in the 8YSZ and their grains were well connected compared to $La_2Zr_2O_7$, as shown in Figs. 7e and 7f.

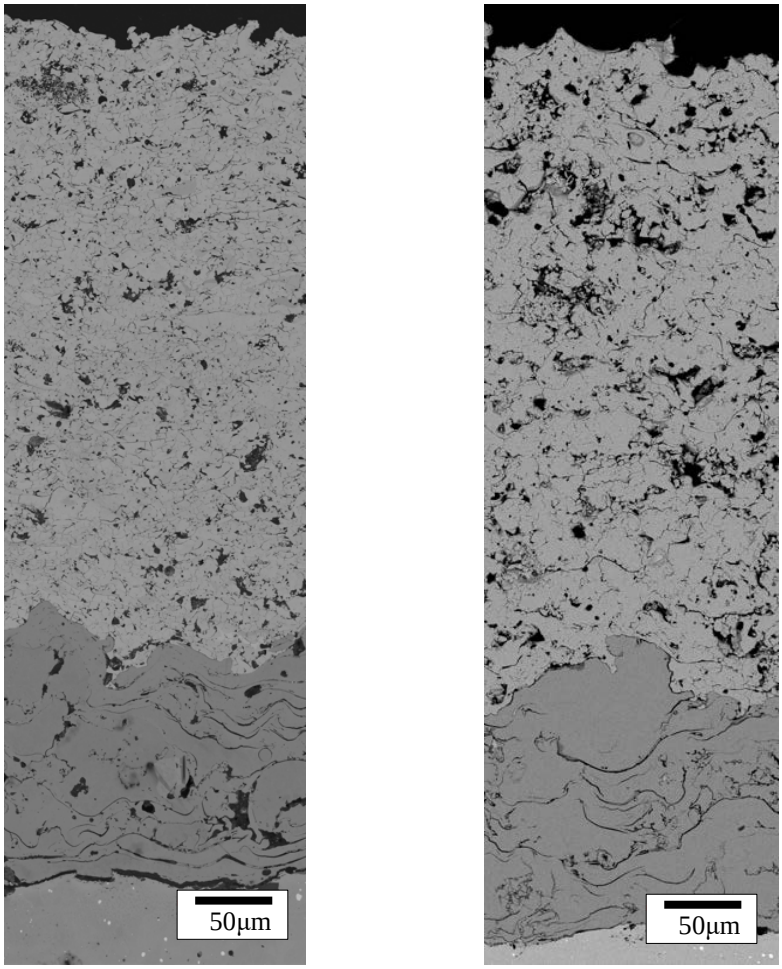

(a) (b)

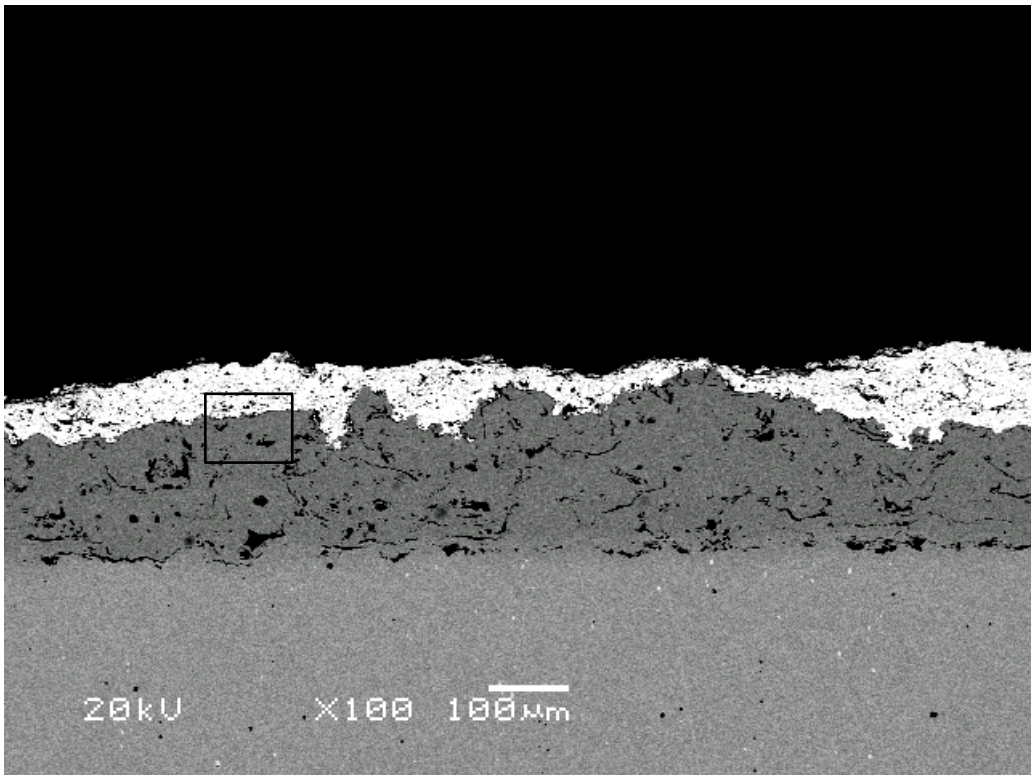

(c)

(c) 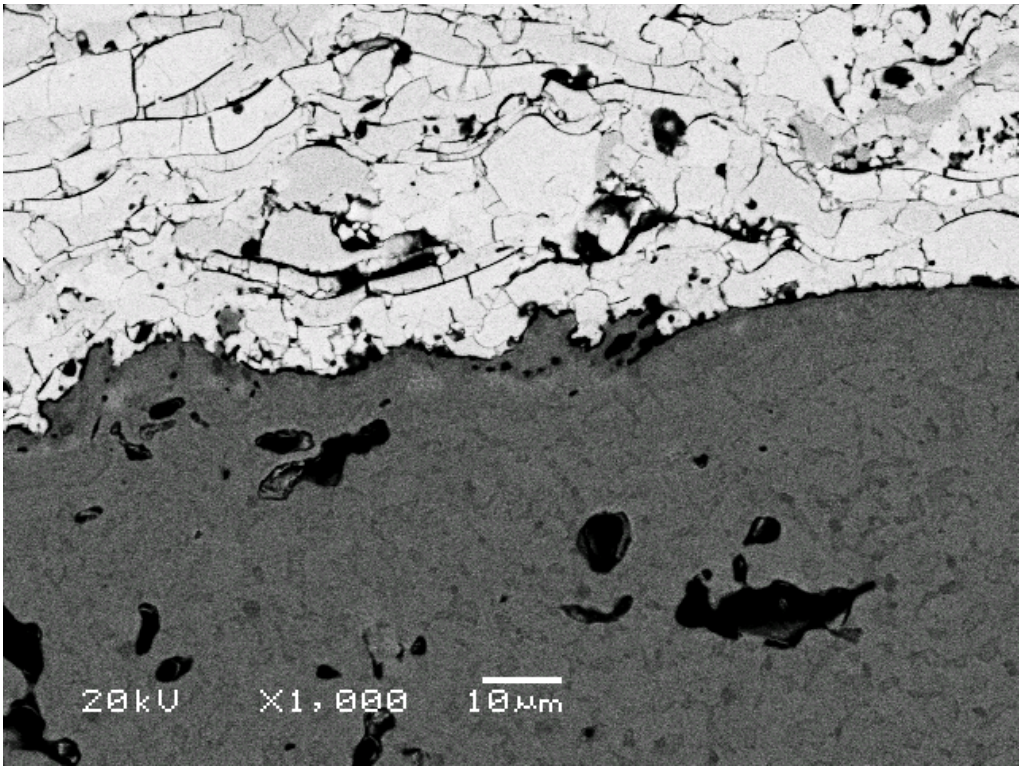

(d)

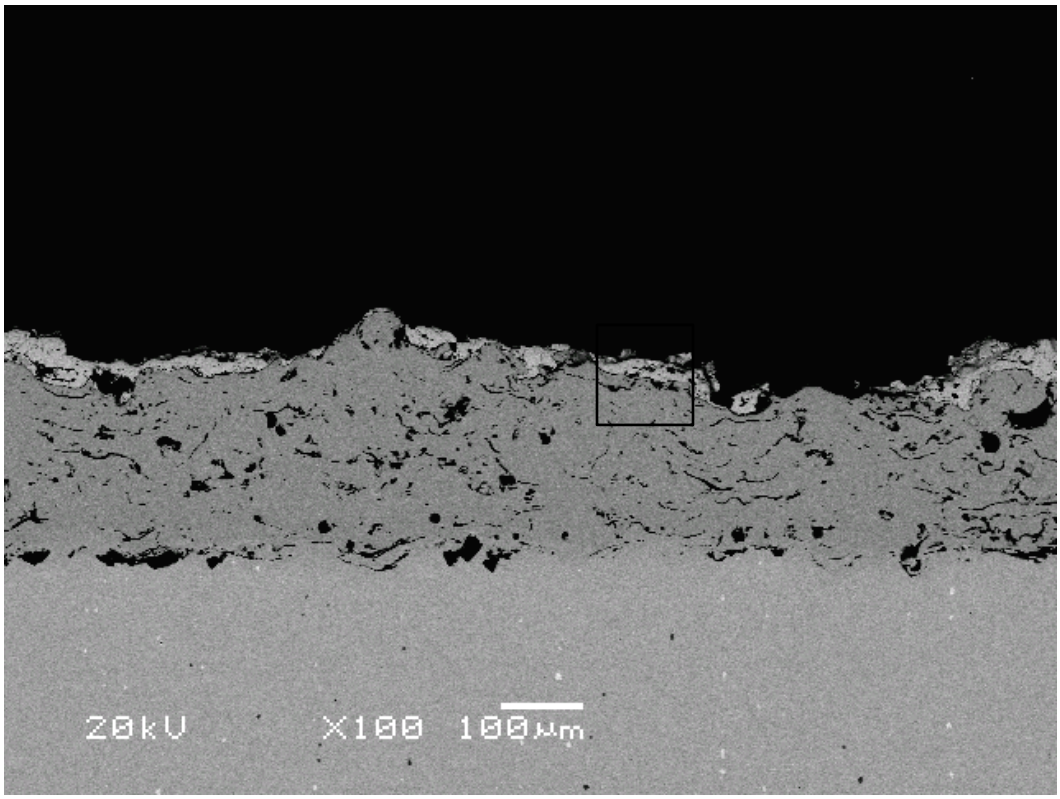

(e)

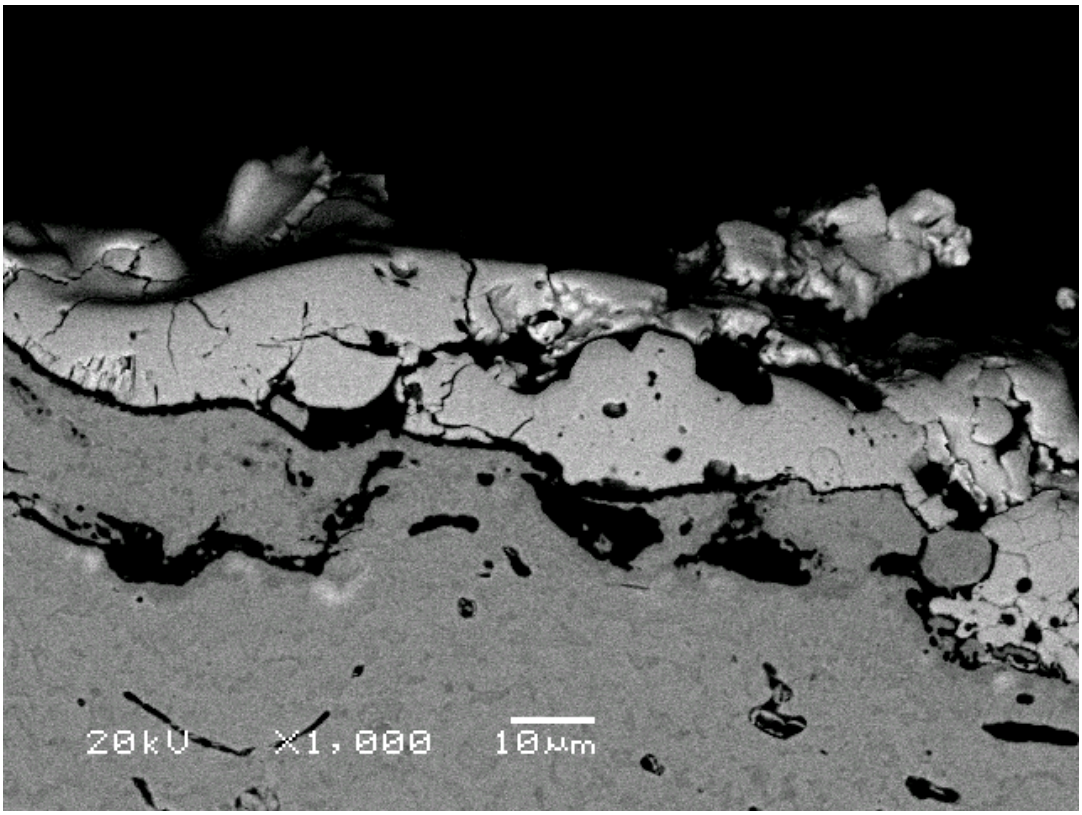

(f)

Fig. 7. Back-scattered electron SEM images of interface layer in SCL $La_2Zr_2O_7$ and 8YSZ before and after adhesive strength tests. (a) Porous $La_2Zr_2O_7$ before the test, (b) Porous 8YSZ before the test, (c) Porous $La_2Zr_2O_7$ after the test, (d) Magnified porous $La_2Zr_2O_7$ microstructure in the block region in (c), (e) Porous 8YSZ coating after the test, (f) Magnified porous 8YSZ microstructure in the block region in (e).

Since the sprayed coating samples were cooled in ambient environment from the elevated deposition temperatures, thermal residual stress was originated in the TBC multilayers, due to thermal expansion difference in each TBCs layer. The residual stresses are generated mainly from the strain mismatch between the coating layers and the substrate when the TBC

systems are cooled from high temperatures to room temperature. When the coatings are cooled from high temperatures, the substrate shrinks more than the coatings due to substrate's higher coefficient of thermal expansion.

In this study, an analytical model proposed by Zhang *et al.* is adopted to understand the residual stress distribution in the coatings, as described below [24, 25]. Considering the displace compatibility, compressive stress is generated in the ceramic coating layers and tension stress is generated in the superalloy substrate. To calculate the residual stress in multiple layer coatings, the interface between the substrate and the bond coat is defined as the origin line, where z=0. The distance from layers i to substrate is defined as h_i [24, 26, 27]. The thermal residual stress in the substrate and i^{th} coating layer, which is related to the misfit strain ε_i and bending curvature K, can be expressed [24, 25]:

$$\sigma_s = E_s\left[\varepsilon_s + K\left(z+\delta\right)\right] \quad (-ts \le z \le 0) \tag{1}$$

$$\sigma_i = E_i\left[\varepsilon_i + K\left(z+\delta\right)\right] \quad (1 \le i \le n,\ h_{i-1} \le z < h_i) \tag{2}$$

where E_s and E_i are the Young's modulus of substrate and i^{th} coating layer. δ is the distance from the bending axis, where the bending strain is zero. ε_i, ε_s, K and δ can be individually expressed by[25]:

$$\varepsilon_i = \Delta\alpha\Delta T + \sum_{k=1}^{n}\frac{E_k t_k}{E_s t_s}(\alpha_k - \alpha_i)\Delta T \tag{3}$$

$$\varepsilon_s = -\sum_{i=1}^{n}\frac{E_i t_i}{E_s t_s}\Delta\alpha\Delta T \tag{4}$$

$$\delta = \frac{t_s}{2} - \sum_{i=1}^{n}\frac{E_i t_i}{E_s t_s}\left(2h_{i-1} + t_i\right) \tag{5}$$

$$K = -\sum_{i=1}^{n} \frac{6E_i t_i \Delta\alpha \Delta T}{E_s {t_s}^2} \quad (6)$$

where α is the coefficient of thermal expansion (CTE), k is the ceramic coating layers range from 1 to n, t_i is the thickness of i^{th} layer.

The calculated thermal residual stress from equations (1) ~ (6), along with Townsend's thermal stress model, is shown in Fig. 8 [26]. The compressive residual stress difference at the interface of SCL $La_2Zr_2O_7$ coating was about 3 GPa larger than that of SCL 8YSZ. Due to the residual stress discrepancy, there were more defects, such as grain boundaries and pores, near the interface area of SCL $La_2Zr_2O_7$ TBCs, which is consistent to the SEM images in Fig. 7 (b) and (d). Since there were more distributed grain boundaries in $La_2Zr_2O_7$ than 8YSZ, so the $La_2Zr_2O_7$ ceramic layers were easily to break. Besides, comparing to the interface, the $La_2Zr_2O_7$ layers were much weaker due to their lower fracture toughness and scattered boundaries[21], so the spallation occurred inside the $La_2Zr_2O_7$ coating layer instead of interface. Similarly, the adhesive strength in $La_2Zr_2O_7$ TBC samples was lower than that of 8YSZ, which showed that the spallation occurred much easier in the $La_2Zr_2O_7$ coating than 8YSZ.

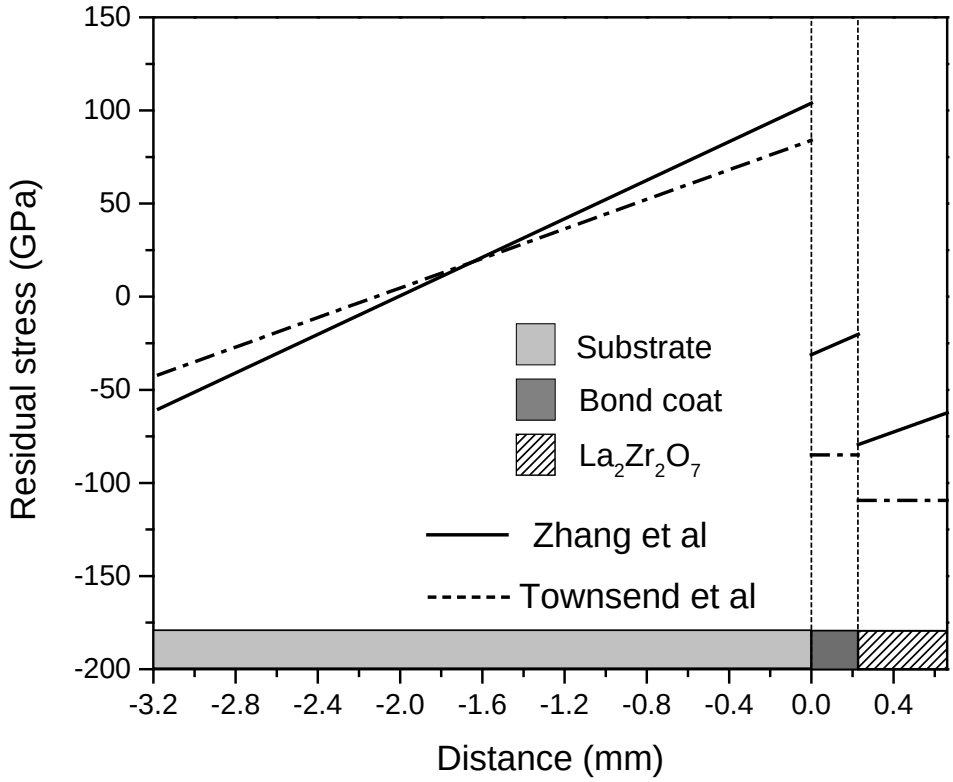
150
100
50
0
-50
-100
-150
-200
Residual stress (GPa)
-3.2
-2.8
-2.4
-2.0
-1.6
-1.2
-0.8
-0.4
0.0
0.4
Distance (mm)
Substrate
Bond coat
La2Zr2O7
Zhang et al
Townsend et al

(a)

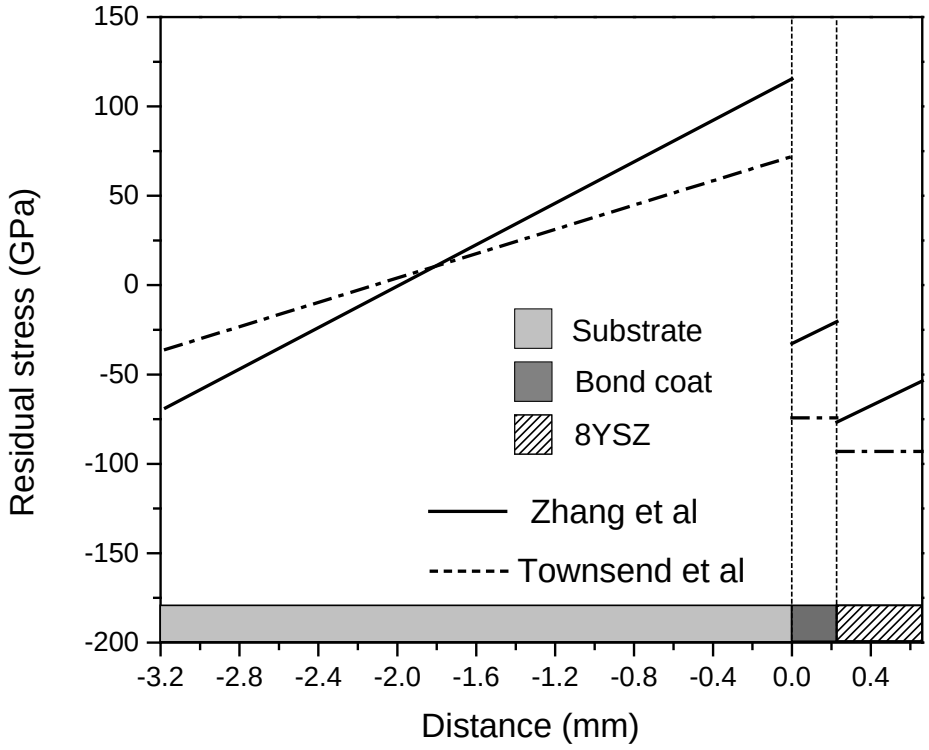

(b)

Fig. 8. Residual stress distributions as a function of coating thickness: (a) residual stress distribution in SCL $La_2Zr_2O_7$ sample and (b) residual stress distribution in SCL 8YSZ sample.

3.4 Erosion test

Fig. 9 summarizes the erosion rate results for the four TBC systems. Sample 1 is SCL porous $La_2Zr_2O_7$. Sample 2 is SCL porous 8YSZ. Sample 3 is DCL porous 8YSZ + $La_2Zr_2O_7$. Sample 4 is DCL dense 8YSZ + $La_2Zr_2O_7$. The SCL porous 8YSZ coating samples had the lowest erosion rate, which was about only half of the other samples erosion rate. The erosion rates of all $La_2Zr_2O_7$ coating layers were higher than 8YSZ. However, the

DCL porous 8YSZ + $La_2Zr_2O_7$ had a lower erosion rate than other SCL and DCL $La_2Zr_2O_7$ coatings, suggesting porous 8YSZ serves as a stress relief buffer layer.

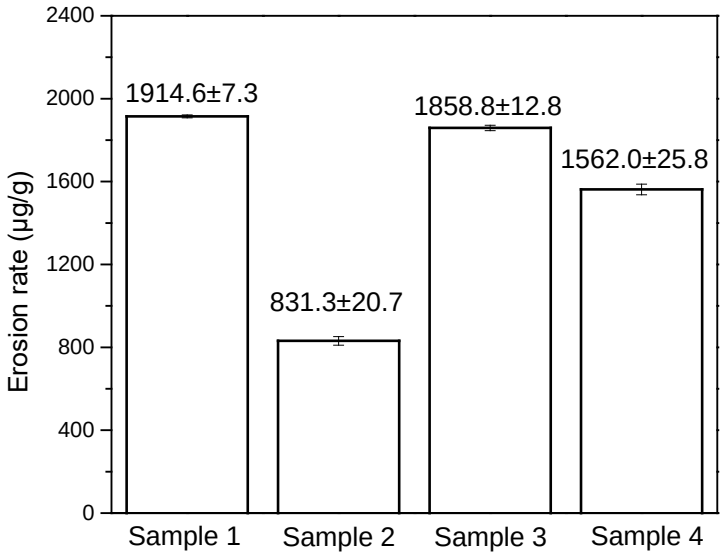

Fig. 9. Erosion rate results. Samples 1, 2, 3, and 4 indicate SCL porous $La_2Zr_2O_7$, SCL porous 8YSZ, DCL porous 8YSZ + $La_2Zr_2O_7$, and DCL dense 8YSZ + $La_2Zr_2O_7$, respectively.

Figure 10 shows the optical micrographs of TBCs samples after the erosion experiments. Although the single layered 8YSZ TBCs had a lower erosion rate, the center of the coating was penetrated, as shown in Fig. 10 (a). The substrate of sample 1 was exposed, so this small hole can lead to failure of the whole coating system. Similarly, the top coatings of sample 2 and 3 were penetrated, as shown in Fig. 10 (b) and (c). Fig. 10 (c) shows two concentric ellipses, which separated $La_2Zr_2O_7$, porous 8YSZ, and substrate. The dark solid ellipse area in Fig. 10 (d) is the dense 8YSZ layer, which was not penetrated. However, all $La_2Zr_2O_7$ top coating layers and a few 8YSZ layers were removed in this ellipse region.

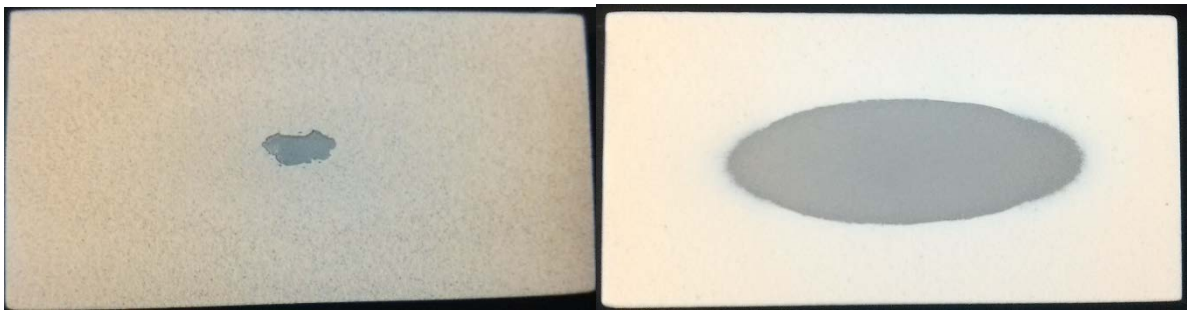

(a) (b)

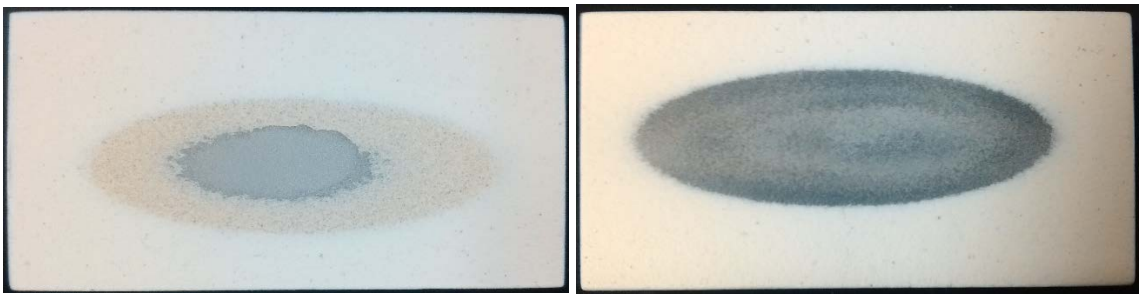

(c) (d)

Fig. 10. Optical micrographs of the erosion test samples: (a) sample #1, SCL porous 8YSZ, (b) sample #2, SCL $La_2Zr_2O_7$, (c) sample #3, DCL Porous 8YSZ + $La_2Zr_2O_7$, and (d) sample #4, DCL dense 8YSZ + $La_2Zr_2O_7$

The cross sectional SEM images of the erosion samples, passing through the erosion areas, are shown in Fig. 11. As shown in Fig. 11 (a), although the erosion hole was relatively small, the porous 8YSZ top coat in this area was almost delaminated from the substrate. As shown in Fig. 11 (b), the removed part was large in the $La_2Zr_2O_7$ coating layer, but both sides were still connected with the substrate. For the DCL porous 8YSZ plus $La_2Zr_2O_7$ coatings shown in Fig. 11 (c), both double layered coatings were removed in the center. More porous 8YSZ material was left than $La_2Zr_2O_7$. The interfaces between each

layers were connect well. As shown in Fig. 11 (d), although there was a big loss of $La_2Zr_2O_7$, the dense 8YSZ layer was almost intact. The interface between dense 8YSZ and substrate was also well connected.

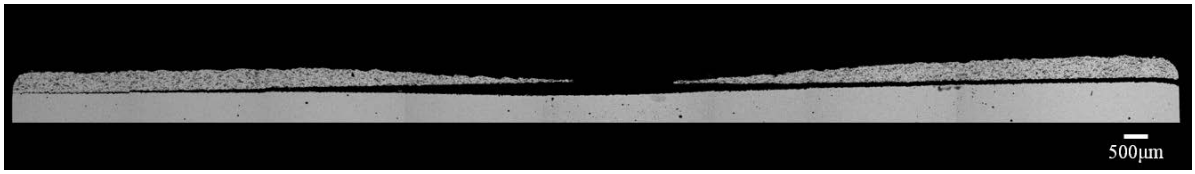

(a)

(b)

(c)

(d)

Fig. 11. Cross sectional back-scattered electron SEM images of the erosion panels: (a) sample #1, SCL porous 8YSZ, (b) sample #2, SCL $La_2Zr_2O_7$, (c) sample #3, DCL Porous 8YSZ + $La_2Zr_2O_7$, and (d) sample #4, DCL dense 8YSZ + $La_2Zr_2O_7$.

The SEM images at the edge of the erosion areas are shown in Fig. 12. As shown in Fig. 12 (a) and (b), both SCL porous 8YSZ and SCL $La_2Zr_2O_7$ layers were delaminated from the substrate in the interfacial area. However, the double layered coatings had better sound interfaces, as shown in Fig. 12 (c) and (d).

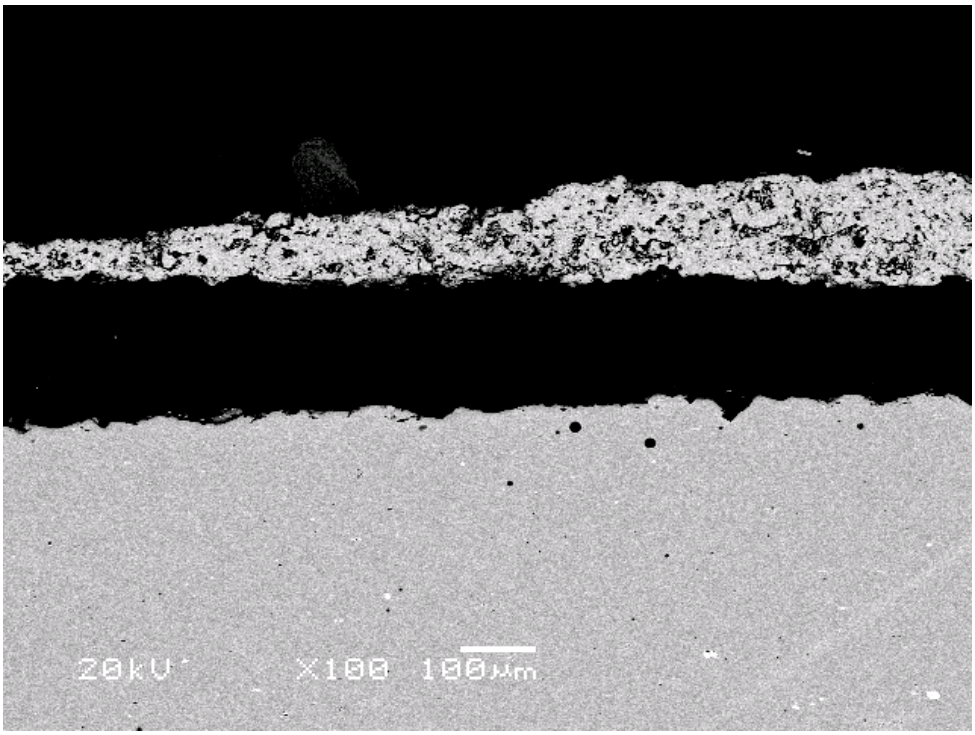

(a)

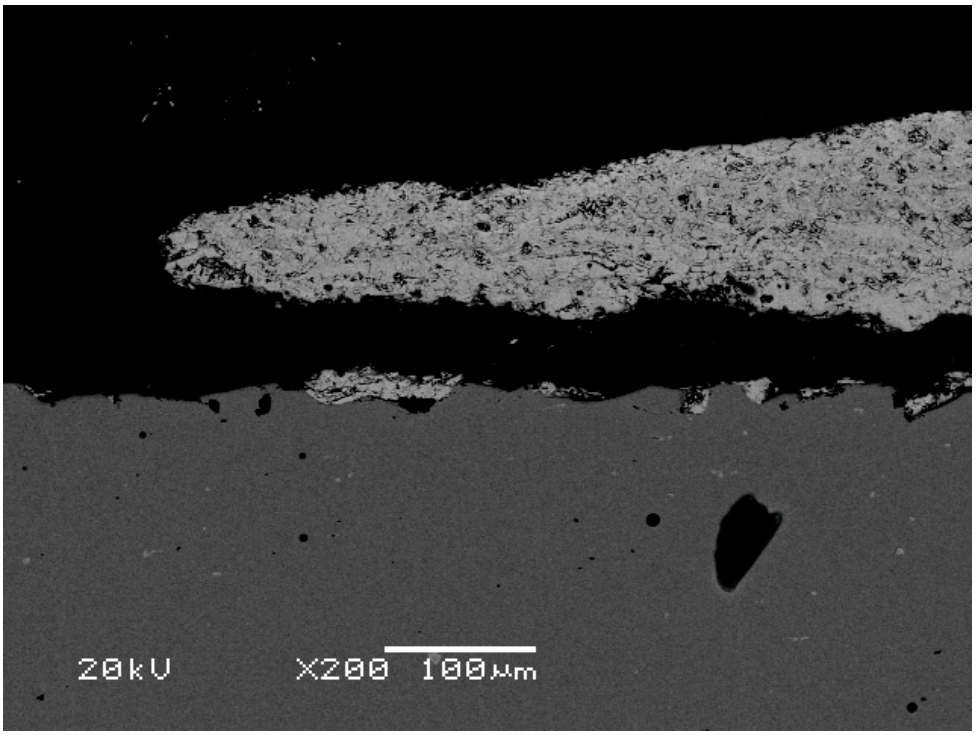

(b)

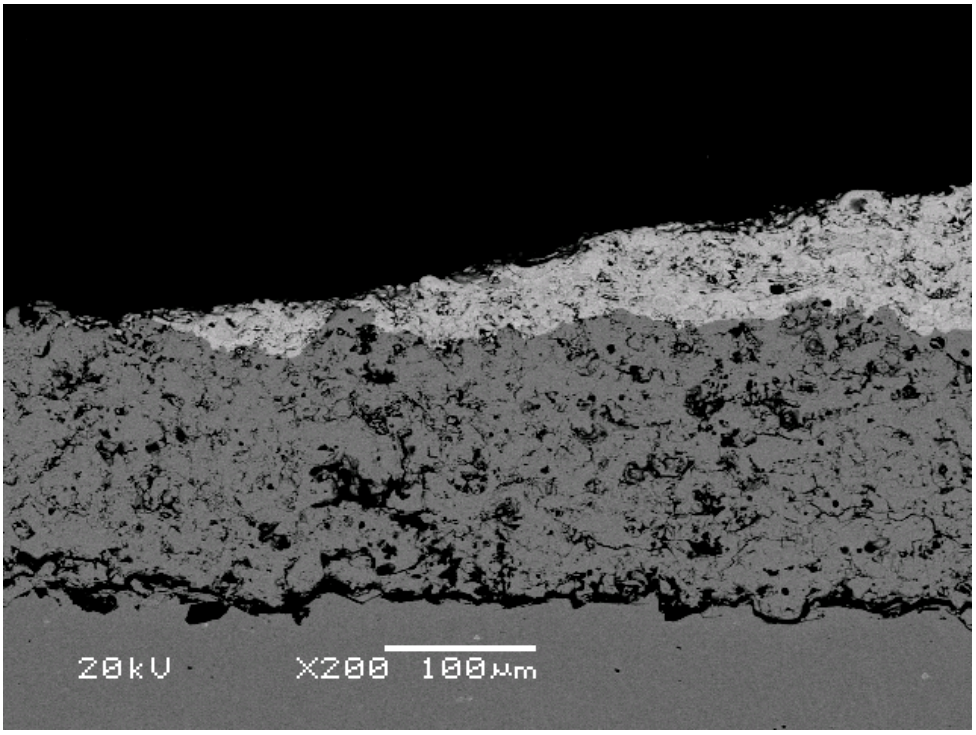

(c)

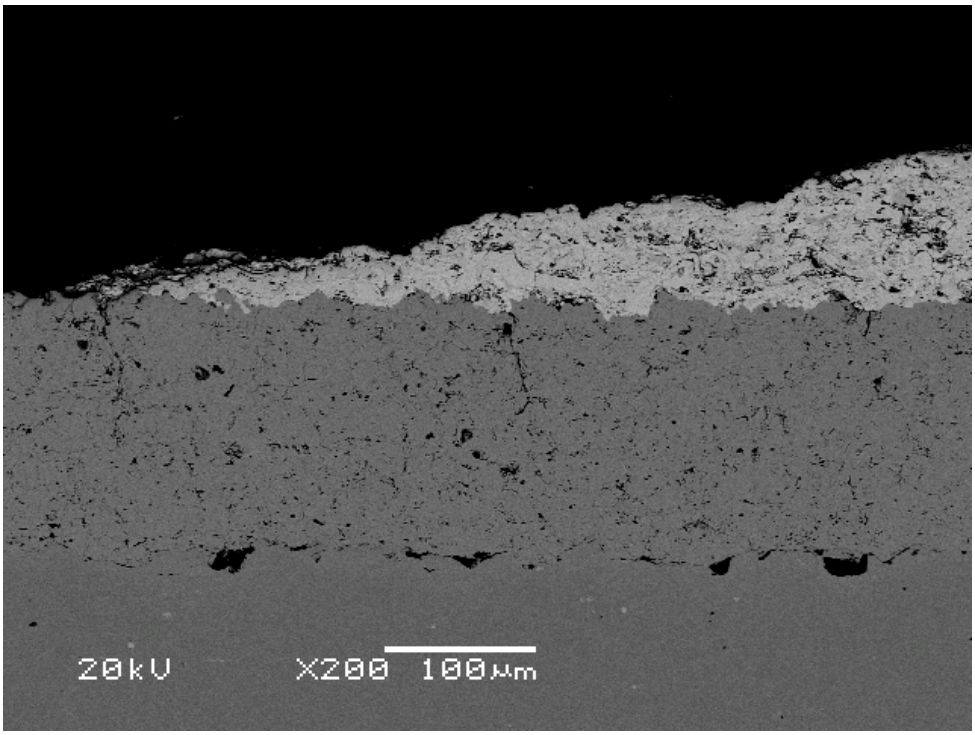

(d)

Fig. 12. Cross sectioal back-scattered electron SEM images at the edge of the erossion are: (a) sample #1, SCL porous 8YSZ, (b) sample #2, SCL $La_2Zr_2O_7$, (c) sample #3, DCL Porous 8YSZ + $La_2Zr_2O_7$, and (d) sample #4, DCL dense 8YSZ + $La_2Zr_2O_7$

The 8YSZ coatings showed a better erosion resistance than $La_2Zr_2O_7$ coatings, mainly because the fracture toughness of 8YSZ was higher than $La_2Zr_2O_7$. Besides, the hardness values of dense 8YSZ layers were higher than other TBCs coat layers, as discussed above, so the erosion rate of this layer was lowest.

An erosion model can be applied to brittle materials such as TBCs, which focuses on the relationship between TBC material properties, such as Young's modulus and fracture

toughness, and the erosion process conditions, such as impact velocity and abrasive particle size [28-31]. It is necessary to determine whether an impinging particle will initiate cracks in the target material. The velocity threshold is used to express the critical condition to initiate the crack. Wellman proposed that the critical velocity for the erosion can be given by [32]:

$$V_{crit} = 105 \frac{E^{3/4} K_{IC}^{3}}{H^{13/4} \rho^{1/2} R^{3/2}} \quad (7)$$

where E is Young's modulus, H is hardness, K_{IC} is fracture toughness, ρ is the density of the erodent particle and R is the particle radius.

The calculated critical erodent velocities for each sample are shown in Fig. 13. The critical velocities of $La_2Zr_2O_7$ coating layer were much lower than that of 8YSZ, so the erosion rate of SCL $La_2Zr_2O_7$ TBCs was larger than SCL 8YSZ TBCs. Comparing sample 3 DCL porous 8YSZ+ $La_2Zr_2O_7$ and sample 4 DCL dense 8YSZ+ $La_2Zr_2O_7$, the critical velocity of top layer $La_2Zr_2O_7$ in sample 4 was greater than sample 3, so the sample 3 had a larger erosion rate than sample 4.

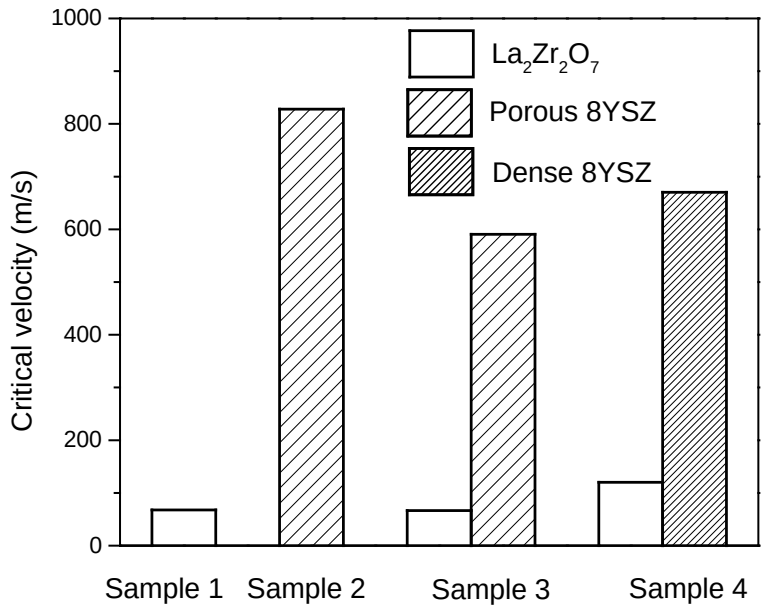

Fig. 13. Critical erodent velocitis of all erosion samples.

Equation 7 provides a possiblity of evalating erosion resistance without conducting erosion experiment. As shown in Fig. 14, a linear fitting (R^2=0.224) between the inverse of critical erosion velocity and experimentally mesured erosion rate, shows a general linear dependency, with the relationship 1/Vcrit (s/m) =8.87×10 (erosion rate, ug/g) – 0.006. Therefore, it becomes possible to predict erosion resistance using Equation 7 along with the physical propertis, without doing the actual experiments.

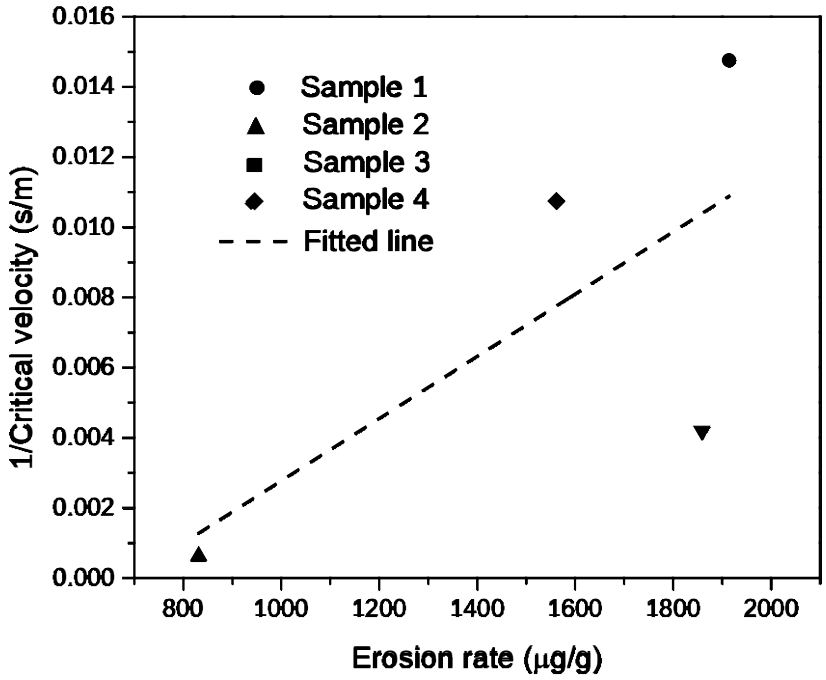

Fig. 14. Correlation between the inverse of the critical velocity and erosion rate.

4. Conclusions

Single layered and double layered $La_2Zr_2O_7$ and 8YSZ TBC specimens were investigated in terms of their thermomechanical properties. The conclusions are summarized as follows.

1. Single layered and double layered $La_2Zr_2O_7$ TBC coatings had less thermal cycling lives than 8YSZ coatings in the TGMF tests. The main reason is the lower fracture toughness of $La_2Zr_2O_7$. Besides, the large CTE mismatch between 8YSZ and $La_2Zr_2O_7$ led to high residual stress. Crack occurred near the interface between the 8YSZ and $La_2Zr_2O_7$ layers.

2. 8YSZ TBCs had higher adhesive strength and erosion rate than $La_2Zr_2O_7$ TBCs, independent of structural design. This is because 8YSZ has higher fracture toughness and critical abrative velodcity than $La_2Zr_2O_7$.

3. The DCL porous 8YSZ + $La_2Zr_2O_7$ had a lower erosion rate than other SCL and DCL $La_2Zr_2O_7$ coatings, suggesting porous 8YSZ serves as a stress relief buffer layer.

4. A new approach of evaluating erosion resistance without conducing erosion test is proposed.

5 Acknowledgement

This work was supported by the financial support provided by the United State Department of Energy (Grant No. DE-FE0008868, program manager: Richard Dunst) and Indiana University - Purdue University Indianapolis Research Support Funds Grant (RSFG) and International Research Development Fund (IRDF). Y.G.J also acknowledges the financial support by “Human Resources Program in Energy Technology” of the Korea Institute of Energy Technology Evaluation and Planning (KETEP), granted financial resource from the Ministry of Trade, Industry & Energy, Republic of Korea. (No. 20174030201460).

References

[1] J. H. Perepezko, "The Hotter the Engine, the Better," *Science*, vol. 326, pp. 1068–1069, November 20, 2009 2009.

[2] R. Vassen, X. Cao, F. Tietz, D. Basu, and D. Stover, "Zirconates as New Materials for Thermal Barrier Coatings," *Journal of the American Ceramic Society*, vol. 83, pp. 2023–2028, 2000.

[3] X. Q. Cao, R. Vassen, and D. Stoever, "Ceramic materials for thermal barrier coatings," *Journal of the European Ceramic Society*, vol. 24, pp. 1–10, 2004.

[4] K. Bobzin, N. Bagcivan, T. Brögelmann, and B. Yildirim, "Influence of temperature on phase stability and thermal conductivity of single- and double-ceramic-layer EB–PVD TBC top coats consisting of 7YSZ, $Gd_2Zr_2O_7$ and $La_2Zr_2O_7$," *Surface and Coatings Technology*, vol. 237, pp. 56–64, 12/25/ 2013.

[5] F. H. Brown and P. O. L. Duwez, "The Systems Zirconia-Lanthana and Zirconia-Neodymia," *Journal of the American Ceramic Society*, vol. 38, pp. 95–101, 1955.

[6] R. Vaßen, F. Traeger, and D. Stöver, "New Thermal Barrier Coatings Based on Pyrochlore/YSZ Double-Layer Systems," *International Journal of Applied Ceramic Technology*, vol. 1, pp. 351–361, 2004.

[7] R. Vassen, X. Cao, F. Tietz, D. Basu, and D. Stöver, "Zirconates as New Materials for Thermal Barrier Coatings," *Journal of the American Ceramic Society*, vol. 83, pp. 2023–2028, 2000.

[8] J. Feng, B. Xiao, R. Zhou, W. Pan, and D. R. Clarke, "Anisotropic elastic and thermal properties of the double perovskite slab-rock salt layer $Ln_2SrAl_2O_7$ (Ln = La, Nd, Sm, Eu, Gd or Dy) natural superlattice structure," *Acta Materialia*, vol. 60, pp. 3380–3392, 5// 2012.

[9] C. Wang, Y. Wang, S. Fan, Y. You, L. Wang, C. Yang, *et al.*, "Optimized functionally graded $La_2Zr_2O_7$/8YSZ thermal barrier coatings fabricated by suspension plasma spraying," *Journal of Alloys and Compounds*, vol. 649, pp. 1182–1190, 11/15/ 2015.

[10] T. Liu, X. Chen, G.-J. Yang, and C.-J. Li, "Properties evolution of plasma-sprayed $La_2Zr_2O_7$ coating induced by pore structure evolution during thermal exposure," *Ceramics International*, vol. 42, pp. 15485–15492, 2016/11/01/ 2016.

[11] S. Sivakumar, K. Praveen, G. Shanmugavelayutham, S. Yugeswaran, and J. Mostaghimi, "Thermo-physical behavior of atmospheric plasma sprayed high porosity lanthanum zirconate coatings," *Surface and Coatings Technology*, vol. 326, pp. 173–182, 2017/10/15/ 2017.

[12] G. Lyu, B. G. Kim, S.-S. Lee, Y.-G. Jung, J. Zhang, B.-G. Choi, *et al.*, "Fracture behavior and thermal durability of lanthanum zirconate-based thermal barrier coatings with buffer layer in thermally graded mechanical fatigue environments," *Surface and Coatings Technology*, vol. 332, pp. 64–71, 2017/12/25/ 2017.

[13] E. Bakan and R. Vaßen, "Ceramic Top Coats of Plasma-Sprayed Thermal Barrier Coatings: Materials, Processes, and Properties," *Journal of Thermal Spray Technology*, vol. 26, pp. 992-1010, August 01 2017.

[14] J. Zhang, X. Guo, Y.-G. Jung, L. Li, and J. Knapp, "Lanthanum Zirconate Based Thermal Barrier Coatings: A Review," *Surface and Coatings Technology*, 2016.

[15] L. Wang, Y. Wang, X. G. Sun, J. Q. He, Z. Y. Pan, and C. H. Wang, "Finite element simulation of residual stress of double-ceramic-layer $La_2Zr_2O_7$/8YSZ thermal barrier coatings using birth and death element technique," *Computational Materials Science,* vol. 53, pp. 117–127, 2012/02/01/ 2012.

[16] F. Cernuschi, C. Guardamagna, S. Capelli, L. Lorenzoni, D. E. Mack, and A. Moscatelli, "Solid particle erosion of standard and advanced thermal barrier coatings," *Wear,* vol. 348-349, pp. 43–51, 2016/02/15/ 2016.

[17] B. Baufeld, M. Bartsch, and M. Heinzelmann, "Advanced thermal gradient mechanical fatigue testing of CMSX-4 with an oxidation protection coating," *International Journal of Fatigue,* vol. 30, pp. 219–225, 2008/02/01/ 2008.

[18] M. Bartsch, B. Baufeld, S. Dalkiliç, L. Chernova, and M. Heinzelmann, "Fatigue cracks in a thermal barrier coating system on a superalloy in multiaxial thermomechanical testing," *International Journal of Fatigue,* vol. 30, pp. 211–218, 2// 2008.

[19] J. Zhang, J. Yu, X. Cheng, and S. Hou, "Thermal expansion and solubility limits of cerium-doped lanthanum zirconates," *Journal of Alloys and Compounds,* vol. 525, pp. 78–81, 6/5/ 2012.

[20] A. G. Evans, D. R. Mumm, J. W. Hutchinson, G. H. Meier, and F. S. Pettit, "Mechanisms controlling the durability of thermal barrier coatings," *Progress in Materials Science,* vol. 46, pp. 505–553, 2001.

[21] K. Jiang, S. Liu, G. Ma, and L. Zhao, "Microstructure and mechanical properties of $La_2Zr_2O_7$–$(Zr_{0.92}Y_{0.08})O_{1.96}$ composite ceramics prepared by spark plasma sintering," *Ceramics International,* vol. 40, pp. 13979–13985, 11// 2014.

[22] M. Gell and E. Jordan, *Bond strength and stress measurements in thermal barrier coatings*, 1995.

[23] G. K. Beshish, C. W. Florey, F. J. Worzala, and W. J. Lenling, "Fracture toughness of thermal spray ceramic coatings determined by the indentation technique," *Journal of Thermal Spray Technology,* vol. 2, pp. 35–38, 1993/03/01 1993.

[24] C. H. Hsueh, "Thermal stresses in elastic multilayer systems," *Thin Solid Films,* vol. 418, pp. 182–188, 10/15/ 2002.

[25] X. C. Zhang, B. S. Xu, H. D. Wang, and Y. X. Wu, "An analytical model for predicting thermal residual stresses in multilayer coating systems," *Thin Solid Films,* vol. 488, pp. 274–282, 9/22/ 2005.

[26] P. H. Townsend, D. M. Barnett, and T. A. Brunner, "Elastic relationships in layered composite media with approximation for the case of thin films on a thick substrate," *Journal of Applied Physics,* vol. 62, pp. 4438–4444, 1987.

[27] Y. C. Tsui and T. W. Clyne, "An analytical model for predicting residual stresses in progressively deposited coatings Part 1: Planar geometry," *Thin Solid Films,* vol. 306, pp. 23–33, 8// 1997.

[28] D. B. Marshall, B. R. Lawn, and A. G. Evans, "Elastic/Plastic Indentation Damage in Ceramics: The Lateral Crack System," *Journal of the American Ceramic Society,* vol. 65, pp. 561–566, 1982.

[29] D. Park, M.-W. Cho, and H. Lee, "Effects of the impact angle variations on the erosion rate of glass in powder blasting process," *The International Journal of Advanced Manufacturing Technology,* vol. 23, pp. 444–450, 2004/03/01 2004.

[30] A. P. Verma and G. K. Lal, "A Theoretical Study of Erosion Phenomenon in Abrasive Jet Machining," *Journal of Manufacturing Science and Engineering*, vol. 118, p. 564, 1996.
[31] P. J. Slikkerveer, P. C. P. Bouten, F. H. in't Veld, and H. Scholten, "Erosion and damage by sharp particles," *Wear*, vol. 217, pp. 237–250, 5/15/ 1998.
[32] R. G. Wellman and J. R. Nicholls, "A Monte Carlo model for predicting the erosion rate of EB PVD TBCs," *Wear*, vol. 256, pp. 889–899, 5// 2004.